Periodica Polytechnica Chemical Engineering, 67(2), pp. 242–255, 2023

Synthesis and Characterization of Biphasic Calcium Phosphate Substituted Cerium as a Potential Osteoporotic Bone Filler

Tri Windarti[1*], Limpat Nulandaya[2,3], Widjijono Widjijono[4], Nuryono Nuryono[5]

[1] Chemistry Department, Faculty of Science and Mathematics, Universitas Diponegoro, Jl. Prof. Soedharto SH, 50275 Semarang, Indonesia
[2] Center for Progressive Materials, Technology and Innovation Park, Pavol Jozef Šafárik University, Trieda SNP 1, 041 11 Kosice, Slovak Republic
[3] Institute of Experimental Physics, Slovak Academy of Sciences, Watsonova 47, 040 01 Kosice, Slovak Republic
[4] Department of Dental Biomaterial, Faculty of Dentistry, Universitas Gadjah Mada, Jl. Denta No.1, Sekip Utara, 55281 Yogyakarta, Indonesia
[5] Department of Chemistry, Faculty of Mathematics and Natural Sciences, Universitas Gadjah Mada, Jl. Geografi, Sekip Utara, 55281 Yogyakarta, Indonesia
[*] Corresponding author, e-mail: tri.windarti@lecturer.undip.ac.id

Received: 01 September 2022, Accepted: 23 February 2023, Published online: 28 March 2023

Abstract

Biphasic calcium phosphate substituted cerium (BCP/Ce) is a potential material for osteoporotic bone filler. Synthesis of BCP/Ce was conducted by the sol-gel method. This work aimed to study the influence of cerium as a precursor on the crystal structures, surface properties, and agglomeration of BCP/Ce. A series of samples were prepared by various Ce percentages (0.5–16%) and a constant molar ratio of (Ca + Ce)/P = 1.2. A structural study by Rietveld refinement calculation confirmed that synthesis without Ce produced BCP that contained hydroxyapatite (HA) and β-tricalcium phosphate (β-TCP) at a ratio of 93:7. The presence of Ce increased β-TCP content to 73% for the use of Ce 8%. None of Ca in the HA structure was replaced by Ce. Otherwise, Ce replaced Ca in β-TCP structure by isomorphic substitution at the Wyckoff site of 6a (0,0,-0.085) or Ca (4) position. As the maximum occupancy of Ca (4) = 43%, about 17% of that was substituted by Ce for the use of 14% Ce. Ce was found in two states as Ce^{3+} and Ce^{4+} ions with Ce^{3+}/Ce^{4+} ratio > 1. The presence of Ce on the particle surface caused a change in the particle shape, from plate-like to spherical. The particle size decreased to <100 nm with the increase of Ce content. The rise of Ce content in BCP decreased the luminescent property due to the increase of oxygen vacancies. The negative value of Zeta potential confirms that BCP/Ce surface can accommodate bone cell proliferation.

Keywords

biphasic calcium phosphate, hydroxyapatite, β-tricalcium phosphate, isomorphic substitution, cerium

1 Introduction

Biphasic calcium phosphate (BCP) contains hydroxyapatite (HA, $Ca_{10}(PO_4)_6(OH)_2$) and β-tricalcium phosphate (β-TCP, β-$Ca_3(PO_4)_2$) has been widely studied as a bone substitute material due to its high bioactivity [1–4]. HA, the most stable calcium phosphate compound in a physiological environment is combined with β-TCP that can be dissolved by osteoclast cell activity [5, 6]. The ions released from β-TCP dissolution can be used to form a new bone structure [7], whereas HA acts as a template [8, 9]. The combination of HA and β-TCP can overcome the mechanical strength gap between the host and implant, especially in cases of low bone density treatment such as osteoporotic bone [10–13].

Substituting ions into BCP structure for various purposes has been extensively studied, such as substituting Ca^{2+} with Eu^{3+} to generate a luminescent property, Mg^{2+} to improve calcium phosphate nucleation on the BCP surface, Mn^{2+} to increase BCP's density, and Fe^{3+} to improve BCP's biological behaviors and generate magnetic properties [14–17]. On the other hand, cerium oxide (CeO_2) has been studied as a potential material for the therapy of diseases caused by a high level of reactive oxygen species (ROS), such as osteoporosis, due to its antioxidant properties [18]. Cerium has two oxidation states, 3+ (Ce^{3+} ion) and 4+ (Ce^{4+} ion), with a subsequent low Ce^{3+}/Ce^{4+} reduction potential (~1.52 V) that

Cite this article as: Windarti, T., Nulandaya, L., Widjijono, W., Nuryono, N. "Synthesis and Characterization of Biphasic Calcium Phosphate Substituted Cerium as a Potential Osteoporotic Bone Filler", Periodica Polytechnica Chemical Engineering, 67(2), pp. 242–255, 2023. https://doi.org/10.3311/PPch.21111

allows the interchange of Ce^{3+} and Ce^{4+} state as a regenerative process in a high ROS environment. Combining with Ce, BCP may be applied as a bone substitute material with a regenerative antioxidant property. The spherical shape of BCP/Ce particles is beneficial when used as a powder component of injectable calcium phosphate cement (CPC) [19, 20]. Since a change in the atomic arrangement will affect the material properties, BCP with Ce (BCP/Ce) should be modified to sustain the BCP structure. Oxygen vacancies due to the charge difference of Ca and Ce will produce catalytic reaction spots, a site where the reduction of ROS level may proceed [21, 22].

Literature studies have collected several facts, including substituting 5% Ce into hydroxyapatite (HA) structure produced HA/Ce with a Ce^{3+}/Ce^{4+} ratio of 1.81. That ratio decreased to 0.48 after HA/Ce was exposed to ROS, indicating that Ce in the HA structure can generate antioxidant properties [23]. The HA/Ce properties are depended on the synthesis method. Hydrothermal [24] and coprecipitation [25] methods produced HA/Ce particles with a shape and size that were not supported the proposed property [24], and only a small amount of Ce (X_{Ce} = 0.05) was substituted into the HA structure [25]. Nandha Kumar et al. [26] have reported research on Ce addition while synthesizing β-TCP with a simple deposition method. Besides, up to 100% addition, only 0.23% of Ca in the β-TCP structure was substituted by Ce. The reaction tended to produce CeO_2 instead of β-TCP/Ce.

The Ca^{2+}, Ce^{3+}, and Ce^{4+} have ionic radii of 0.106, 0.114, and 0.097 nm, respectively [27], and the electronegativity of Ca and Ce are 1.00 and 1.12, respectively. These facts make the substitution of Ca in the BCP structure with Ce theoretically possible. However, the crystal lattice of HA and β-TCP are hexagonal with Hermann-Mauguin symmetry space group (H-MSSG) of P63/m (COD-1011242) and rhombohedral with H-MSSG of R 3 c (COD-1517238), respectively. Meanwhile, CeO_2 is fluorite cubic with H-MSSG of F m -3 m (COD-4343161) [28, 29]. The difference in crystal lattice and space group needs a proper synthesis method to generate isomorphic substitution. Due to the charge difference, substituting Ca^{2+} with Ce^{3+} and Ce^{4+} may cause a change in the chemical and surface properties of BCP [30].

In this work, BCP/Ce synthesis as a potential osteoporotic bone filler was carried out by the sol-gel method. Based on the previous work [31], the molar ratio of (Ca + Ce)/P was kept constant at 1.2 due to the hope that the composition of resulted BCP contains more β-TCP than HA. A slow reaction process, low drying temperature, and relatively low firing temperature supported by the similarity of Ce^{3+} and Ca^{2+} properties would allow a maximum isomorphic substitution. According to the importance of surface morphology in bone tissue engineering, cetyltrimethylammonium bromide (CTAB) surfactant was used as a morphology-directing agent. Shiba et al. [32] found that the present of CTAB affects the morphology of HA due to HA crystal nucleation occurred on the surface of CTAB micelles with the interaction sequence $CTA^+–PO_4^{3-}–Ca^{2+}$. Cationic N from CTAB interacts with Ca^{2+} ions in the *a* plane of HA crystals, and interacts with OH^- or PO_4^{3-} in the *c* plane of HA crystals produced rod-like shape particles. First, the influence of cerium on the vibrational energy of the phosphate group was analysed by FTIR. Then, the crystal structure of BCP/Ce was obtained by X-ray diffractometer and the Rietveld refinement method was performed by MAUD software. Lastly, the change in some properties, i.e. luminescent, morphology, and zeta potential, due to the presence of Ce were studied.

2 Experimental

2.1 Preparation of BCP/Ce Powder

Synthesis of BCP/Ce was conducted by sol-gel method. About 6.804 g (50 mmol) of KH_2PO_4 (Merck, 1.37039.1000) and 0.0164 g (0.045 mM) of CTAB (Sigma Aldrich, A6284.0100) was dissolved in double distilled water to produce 50 ml of solution I. The weight of CTAB was adjusted to its critical micelle concentration of 0.9 mM. In another glass flask, a certain amount of $Ca(NO_3)_2 \cdot 4H_2O$ (Merck, 1.02121.0500) and $Ce(NO_3)_3 \cdot 6H_2O$ (Merck, 1.02271.0100) were dissolved in double distilled water that contained 0.0164 g (0.045 mM) CTAB to produce 50 ml of solution II. The concentration of Ca^{2+} + Ce^{3+} in solution II was maintained constant for all synthesis, whereas the concentration of Ce^{3+} (% molar to Ca^{2+}, then written as Ce) was varied to yield ten different compositions. The precursors' concentration, along with their sample codes for all ten compositions, is presented in Table 1, and the same codes are used throughout the paper.

The reaction was conducted by slowly adding solution I into solution II with gentle stirring at room temperature (25 °C). The solution was added with NH_4OH 32% (Merck, 1.05426.2500) to adjust pH > 9. Stirring was continued for 1 hour, and then the mixture aged 48 hours. The formed precipitate was washed with double distilled water until the washing filtrate was neutral, dried in an electric oven at 40 °C for 48 hours, and then continued by firing in the electric furnace at 800 °C for 30 minutes in an air atmosphere.

Table 1 Sample code and reactants composition*

Sample Code	$Ca(NO_3)_2 \cdot 4H_2O$ (g)	$Ce(NO_3)_3 \cdot 6H_2O$ (g)	[Ce] (%)
BCP/Ce0	14.169	-	0
BCP/Ce0.5	14.098	0.130	0.5
BCP/Ce1	14.027	0.261	1
BCP/Ce2	13.885	0.521	2
BCP/Ce4	13.602	1.042	4
BCP/Ce8	13.035	2.084	8
BCP/Ce10	12.752	2.605	10
BCP/Ce12	12.469	3.126	12
BCP/Ce14	12.185	3.647	14
BCP/Ce16	11.902	4.169	16

* KH_2PO_4 was kept constant at 6.804 g and
Ce concentration = Ce/(Ca + Ce) × 100%)

2.2 Characterization

The crystal structure was characterized by an X-Ray Diffractometer (XRD) (Shimadzu type XRD-6000) equipped with monochromatic Cu Kα radiation operated at 40 kW (λ = 1.54 Å) and scanned in the range of 3° ≤ 2θ ≤ 80° with a scan speed of 3°/minute (a scan step degree of 0.02°). The MAUD 2.94 software by Lutterotti et al. [33] was used to perform quantitative phase analysis through Rietveld refinement. The standard Crystallography Information File (CIF) for HA (COD-1011242), β-TCP (COD-1517238), and $CePO_4$(COD-1538086) were obtained from the Crystallography Open Database (COD) website [34–36]. The space group numbers for HA and $CePO_4$ are 176 and 14, respectively. While the space group number of β-TCP is 161 with 18 independent atomic positions: 5 Ca positions (3 in site 18b and 2 in site 6a at one-half occupancy), 3 P positions (2 in site 18b and 1 in site 6a), and 10 O positions (9 in site 18b and 1 in site 6a).

The structure refinement sequence was elaborated as follows. The entire phase's structural parameters were opened to fit the peak position in the first step. Second, the peak height for each phase was optimized from the grain texture and Ce substitution for Ca in β-TCP. Third, all crystallite sizes were opened for peak width refinement. Lastly, these three steps were repeated to obtain more precise values. Every calculation had a maximum of 50 iterations with a fourth-grade polynomial background, and phase composition parameters were free released. The crystal structure was visualized by Vesta software.

The functional groups of synthesized products were identified with Fourier Transform-Infrared (FT-IR) spectrophotometer (Shimadzu Prestige 21) through a KBr pellets method at a wavenumber range of 400–4000 cm^{-1}. X-ray photoelectron spectroscopy (XPS) was measured with Thermo VG Scientific (UK) Multilab 2000 spectrometer. Surface morphology and element distribution were observed by Scanning Electron Microscope (SEM) (Hitachi type SU3500) with a Secondary Electron and Energy Dispersive X-ray (EDX) detector. All samples were coated with gold in a thickness of 1 nm by using Hitachi MC1000 sputter ion. The particle shape was observed with Transmission Electron Microscope (TEM) (JEOL type JEM-1400) using ethanol as a dispersant. The luminescent property was analyzed with Fluorescence Spectrometer (FS) (Hitachi F-2700 FL Spectrophotometer), by emitter at λ = 250 nm. Zeta potential measurement was carried out with the Zetasizer Nano (Malvern type ZEN 5600). Measurements were conducted at room temperature and pH 7. The samples were prepared by diluting in 1% tween 80 (v/v) solution and homogenized in an ultrasonic chamber.

3 Results and discussion

3.1 FT-IR analysis

FT-IR spectra of BCP/Ce0 - BCP/Ce12 are shown in Fig. 1. Meanwhile, the spectra of BCP/Ce14 - BCP/Ce16 were not presented due to the similarity pattern with BCP/Ce12. For BCP/Ce0, the specific vibrational energy of phosphate groups appears as sharp peaks at 1095 and 1033 cm^{-1}, which is attributed to ν3 asymmetric bending P-O. At 972 cm^{-1}, it is confirmed as ν1 stretching P-O [37]. Bending vibration (ν4) O-P-O appears at 601 and 570 cm^{-1} [27, 38]. A broad peak at 3441 cm^{-1} indicates the presence of the hydroxyl group or entrapped water. A peak reinforces this peak at 1643 cm^{-1}, which belongs to the bending vibration energy of H_2O [26]. The presence of Ce in the product influences the PO_4^{3-} group environment so that the vibrational

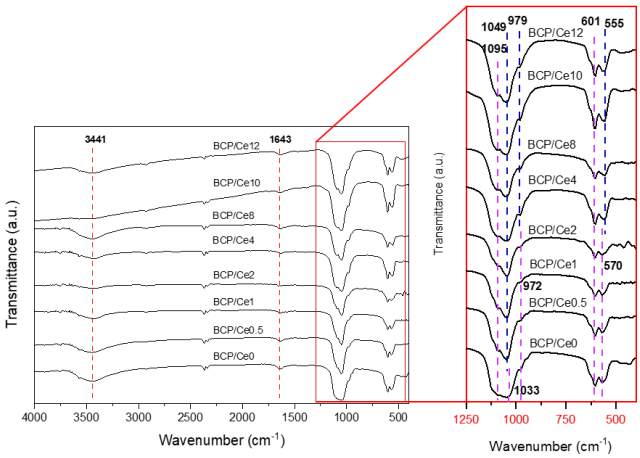

Fig. 1 FTIR spectra of BCP/Ce0 - BCP/Ce12 samples

energy of PO_4^{3-} slightly changes. The *v*3 asymmetric bending P-O shifts from 1033 cm^{-1} to 1049 cm^{-1}, and the peak of *v*1 stretching P-O shifts from 972 to 976 cm^{-1} for BCP/Ce4 - BCP/Ce12 [37]. The peak of *v*4 bending O-P-O shifts from 570 to 555 cm^{-1} for BCP/Ce4 - BCP/Ce12. The Ce-O stretching vibrations should appear at 2930 and 2840 cm^{-1}, but this study's intensity is too small. Ce-O-Ce vibrations between 1180 and 1054 cm^{-1} overlapped with the asymmetric bending P-O peak [39].

3.2 XRD analysis

Fig. 2 shows the diffractogram patterns of all products. The patterns show that at low Ce concentrations, peaks similar to the specific peaks of HA (JCPDS no. 090432) and *β*-TCP (JCPDS no. 090169) appear. Meanwhile, at high Ce concentrations, apart from HA and *β*-TCP peaks, $CePO_4$ peaks also appeared (JCPDS no. 32199). Due to the electron density of $CePO_4$, the diffractogram displayed $CePO_4$ peaks with high intensity compared to the peaks of HA and *β*-TCP [26].

Quantitative information was acquired through refining XRD data using MAUD software to study the products' phase, composition, cell parameters, and crystallite size. The refinement of BCP/Ce0.5 and BCP/Ce10 can be seen in Fig. 3. The refinement for BCP/Ce0.5 yielded χ^2 (goodness of fit parameter) = 1.33 and *Rw* (residual factors) = 15.14%. The value of *Rw*, which is higher than the ideal calculation (<15%), also occurs in BCP/Ce0 (Table 2).

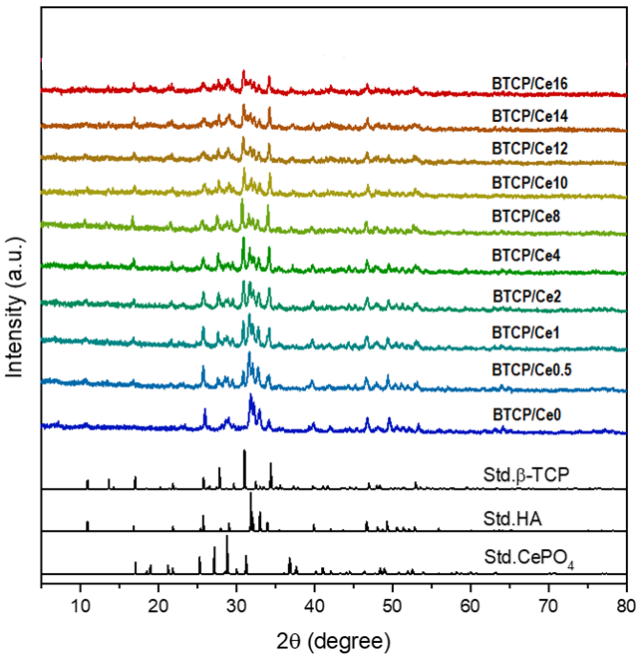

Fig. 2 Diffractogram patterns of BCP/Ce compared to standard HA, *β*-TCP, and $CePO_4$

This phenomenon was noted by Bohner et al. [30], stating that the Rietveld refinement using published XRD *β*-TCP data often resulted in a mismatch. It can happen due to the crystal structure with a lower group space than R3c or the presence of superlattice (a longer-range order).

Synthesis without Ce (BCP/Ce0) produced HA as the major product, in which the HA: *β*-TCP ratio was counted at 93:7 (Fig. 4 (a)). This result differs from previous research [31], in which the same condition produced *β*-TCP as the major product. This may be due to the presence of CTAB in the synthesis process. The cation CTA^+ in CTAB micelles acted as a nucleation site for HA crystal [32]. The HA crystal grew as the sample was heated at 800 °C for 30 minutes. It is known that HA crystal begins to form at 600 °C [40]. In the BCP/Ce0 sample, HA has cell parameters *a* = 9.435 Å, *c* = 6.882 Å, and lattice volume = 531 $Å^3$. Whereas *β*-TCP has cell parameters *a* = 10.489 Å, *c* = 37.268 Å, and lattice volume = 3551 $Å^3$ (Table 2). The *β*-TCP cell parameter is greater than COD-1517238 data and similar to the analysis result with a high-resolution neutron powder diffraction [41].

The fit of diffractogram peaks at low Ce content (BCP/Ce0.5 - BCP/Ce8) showed that the products contain HA and *β*-TCP, while at high Ce content (BCP/Ce10 - BCP/Ce16), the products contain HA, *β*-TCP and $CePO_4$ (Fig. 4 (a)). The addition of Ce significantly increases the *β*-TCP content, in which by the addition of 0.5% Ce (BCP/Ce0.5), the ratios of HA: *β*-TCP changed to 65:35. The maximum percentage of *β*-TCP was obtained in BCP/Ce8 (73%). The $CePO_4$ concentration is higher as the concentration of Ce in the reactants increases.

For all Ce concentrations, no Ca in the HA structure was found to be substituted by Ce. Therefore, the lattice crystal parameters of HA are relatively identical. However, different phenomena happened to *β*-TCP crystals. Among the five positions of Ca in the *β*-TCP crystal, Ce tends to replace Ca (4) position in Wyckoff site 6a or coordinate (0,0,-0.085) (Fig. 5) due to its lower occupancy factor (0.43), higher isotropic thermal parameter, and lower bond valence than the other Ca position [41]. The same phenomenon happened to Mg substituted BCP, in which Mg^{2+} ions tend to incorporate into whitlockite rather than HA [4]. The Rietveld refinement showed that the substitution starts to be detected at synthesis using 8% Ce (BCP/Ce8) (Fig. 4 (b)). As the Ce concentration increase, the occupancy of Ce at the Ca (4) tends to increase as well. As the maximum occupancy of Ca at Ca (4) is 43%, about 17% of that can be replaced by Ce for BCP/Ce14 sample. This value is much greater than

Table 2 Rietveld refinement result by using MAUD

Sample	HA			β-TCP			$CePO_4$					Rietveld agreement factors	
	a (Å)	*c* (Å)	Lattice volume (Å^3)	*a* (Å)	*c* (Å)	Lattice volume (Å^3)	*a* (Å)	*b* (Å)	*c* (Å)	β (°)	Lattice volume (Å^3)	χ^2	*Rw* (%)
BCP/Ce0	9.439	6.883	531	10.475	37.261	3541	-	-	-	-	-	1.40	17.25
BCP/Ce0.5	9.430	6.881	530	10.454	37.401	3540	-	-	-	-	-	1.33	15.14
BCP/Ce1	9.430	6.884	530	10.459	37.414	3544	-	-	-	-	-	1.29	14.16
BCP/Ce2	9.430	6.884	530	10.465	37.451	3552	-	-	-	-	-	1.20	13.36
BCP/Ce4	9.430	6.885	530	10.474	37.485	3561	-	-	-	-	-	1.18	13.01
BCP/Ce8	9.428	6.885	530	10.482	37.520	3570	-	-	-	-	-	1.21	12.50
BCP/Ce10	9.439	6.890	532	10.493	37.553	3581	6.777	6.980	6.448	103.32	297	1.23	13.25
BCP/Ce12	9.436	6.890	531	10.487	37.548	3576	6.769	6.978	6.442	103.35	296	1.20	12.49
BCP/Ce14	9.439	6.885	531	10.488	37.536	3576	6.770	6.977	6.445	103.28	296	1.28	13.17
BCP/Ce16	9.440	6.888	532	10.491	37.536	3578	6.769	6.982	6.444	103.28	296	1.31	13.19

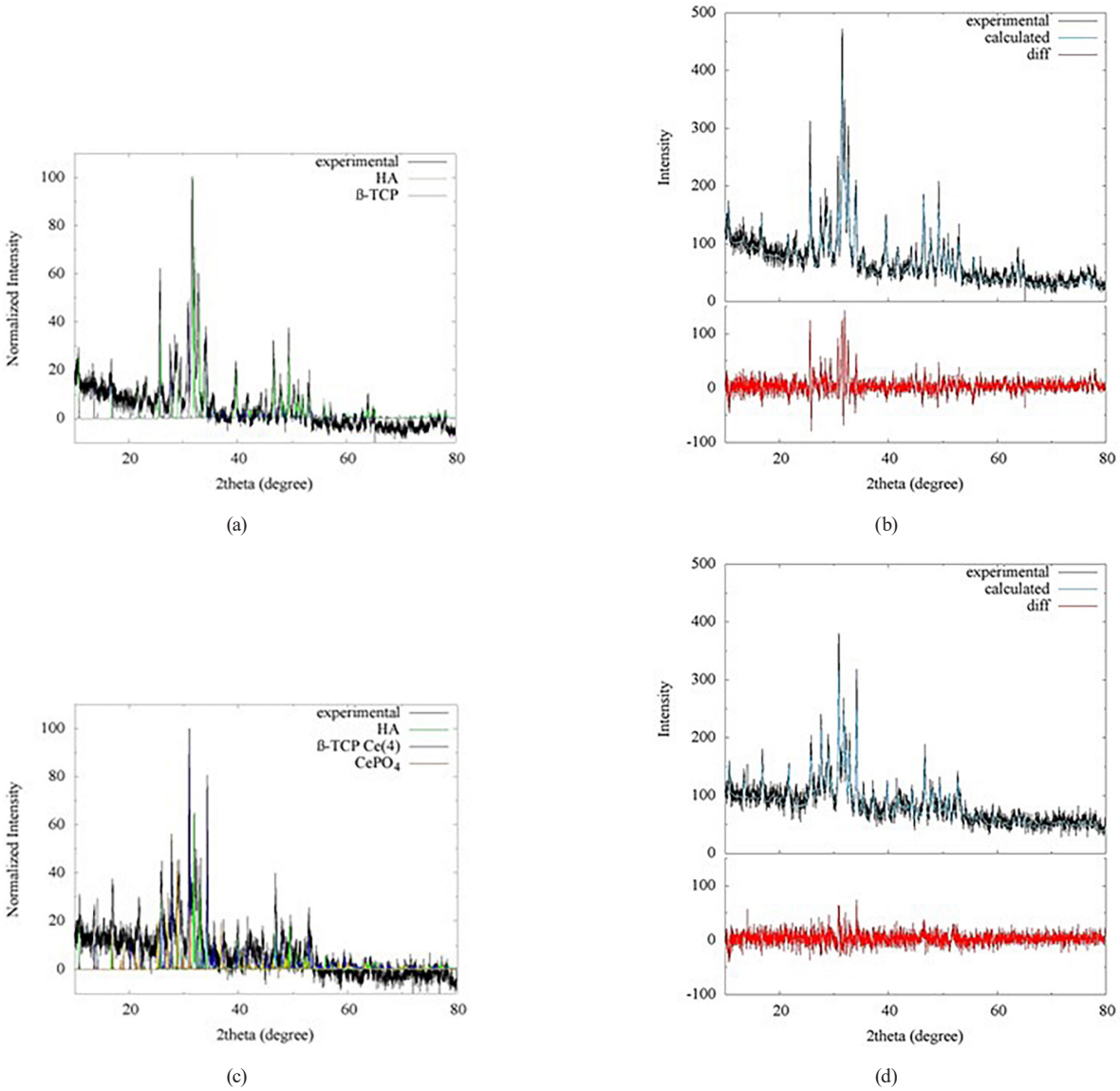

Fig. 3 Rietveld refinement by using MAUD for BCP/Ce0.5: before the refinement (a), after the refinement (b); and for BCP/Ce10: before the refinement (c), after the refinement (d)

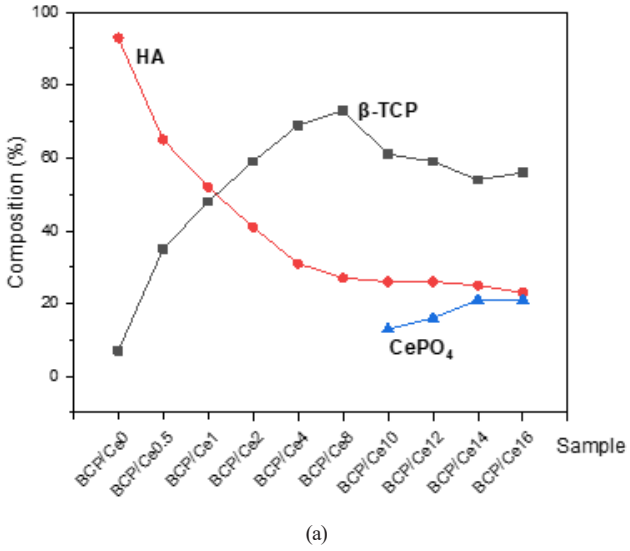

(a)

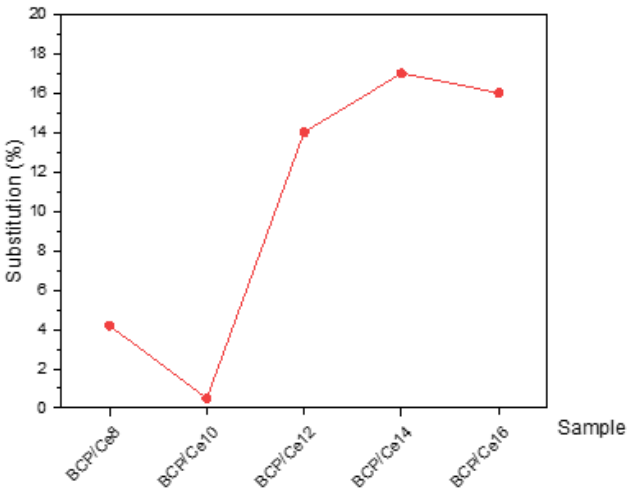

(b)

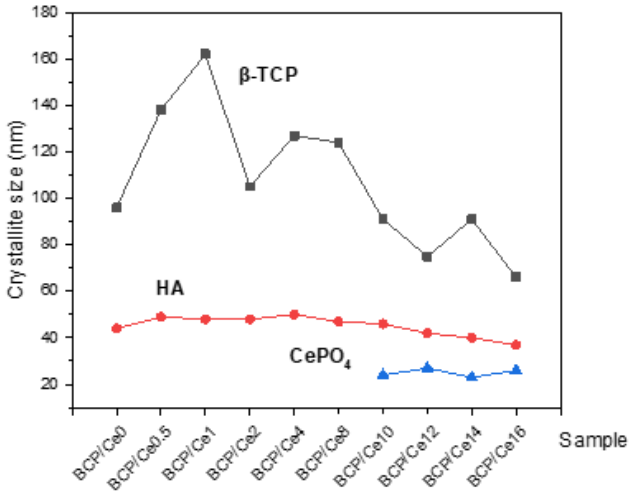

(c)

Fig. 4 Product's composition (a), the substitution of Ce into Ca (4) position (b), and crystallite size (c)

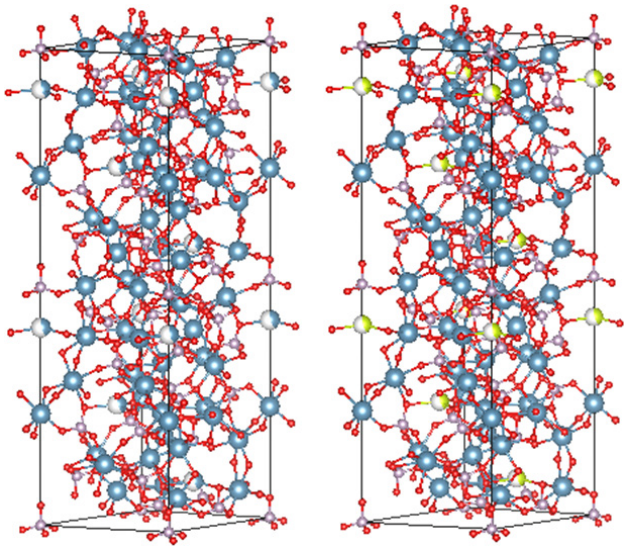

(a) (b)

Fig. 5 Lattice crystal of *β*-TCP (a) and BCP/Ce (b) (P = purple cirle, O = red circle, Ca = blue circle, Ce = green circle)

the amount of Ce substituted into the *β*-TCP structure in the study of Nandha Kumar et al. [26], which only succeeded in replacing Ca with Ce as much as 0.23%.

The presence of Ce slightly changes the lattice parameters *a* and *c* and the lattice volume of *β*-TCP due to the slight difference in ionic radii [42] (Table 2). For the Ce concentration of 0.5–32%, the size of a = 10.454–10.493 Å, c = 37.401–37.553 Å and lattice volume = 3540–3581 Å^3. The BCP/Ce10 sample produced the largest lattice volume. The lattice volume is related to biocompatibility. The larger the crystal lattice, the lower the density, making it easier to degrade. The small difference in the crystal lattice parameters of *β*-TCP proves that the substitution of Ce into the *β*-TCP structure is isomorphic. The crystallite size of *β*-TCP fluctuates to the Ce concentration, which is 66–162 nm. Ce allowed *β*-TCP crystal to grow until 162 nm at BCP/Ce1. Crystallite size *β*-TCP < 100 nm was obtained in BCP/Ce10 - BCP/Ce16 samples. It can be said that synthesis produced a non-uniform trend for *β*-TCP with change in doping concentration. The crystallite size of HA and $CePO_4$ is almost the same for all samples (Fig. 4 (c)).

3.3 XPS analysis

XPS analysis was performed to study the chemical change and Ce oxidation state on the product surface due to the Ce content (Fig. 6 (a)). The binding energy of O *1s*, Ca *2p,* and P *2p* for BCP/Ce0, BCP/Ce4, and BCP/Ce10. The XPS spectra show that the photoemission of O *1s*, Ca *2p,* and P *2p* for the three samples have the same binding energy value.

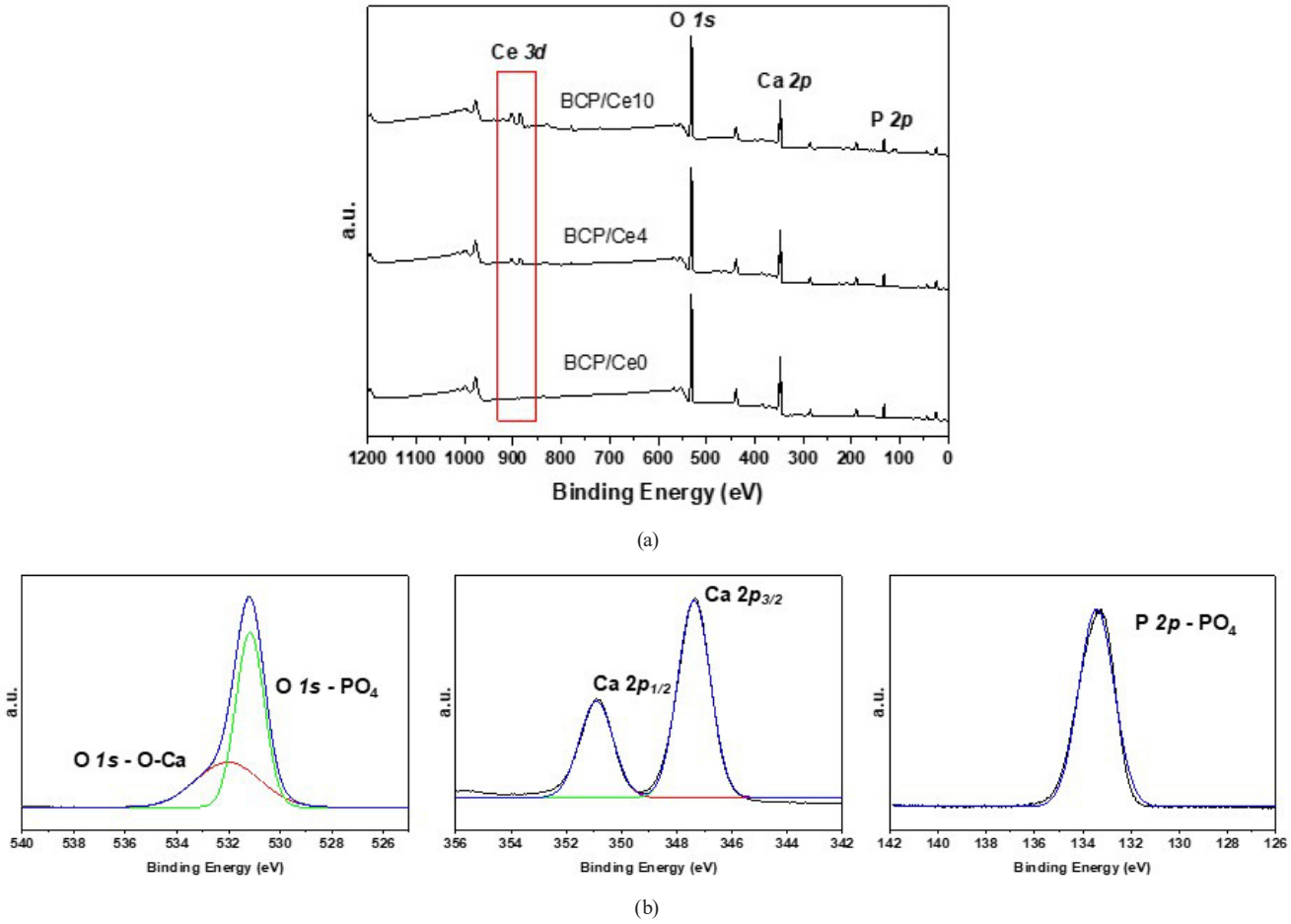

Fig. 6 XPS spectra of BCP/Ce0, BCP/Ce4, and BCP/Ce10 (a) and fitted curves of BCP/Ce0 (b)

Fitted curves of the BCP/Ce0 sample are shown in Fig. 6 (b). The asymmetric peak of O *1s* photoemission is indicated by the O-P (531.2 eV) and O-Ca (532.2 eV) [43]. Doublet peaks of Ca *2p* photoemission are displayed at 350.9 eV and 347.4 eV, confirming Ca $2p_{1/2}$ and Ca $2p_{3/2}$ orbitals. The symmetric peak of Ca *2p* photoemission at 133.4 eV is indicated the binding energy of the PO_4 tetrahedron [26]. The same binding energy of O *1s*, Ca *2p,* and P *2p* for BCP/Ce0, BCP/Ce4, and BCP/Ce10 indicates the substitution of Ca with Ce in the *β*-TCP structure occurs isomorphically. For BCP/Ce4 and BCP/Ce10 samples, specific peaks of Ce *3d* are seen at the binding energy of 875.0–922.0 eV. The intensity of Ce *3d* peaks of the BCP/Ce10 sample is higher than BCP/Ce4's following the Ce content in BCP/Ce.

The deconvolution of Ce *3d* peaks is shown in Fig. 7. For BCP/Ce4, 9 peaks are identified, in which 5 peaks (u, v", u", v", u"') belong to Ce^{4+} and 4 peaks (v°, u°, v', u') belong to Ce^{3+} (Table 3). The main characteristic peaks for Ce^{4+} $3d_{5/2}$ (u") and Ce^{4+} $3d_{3/2}$ (v") appear at binding energy of 917.4 and 898.2 eV. Whereas the characteristic peaks for Ce^{3+} $3d_{3/2}$ (u°) and Ce^{3+} $3d_{5/2}$ (v°) appear at binding energies of 900.0 and 881.8 eV. For BCP/Ce10, 10 peaks are identified, 6 peaks (v, u, v", u", v"', u"') are confirmed as Ce^{4+} and 4 peaks (v°, u°, v', u') are confirmed as Ce^{3+}. The Ce^{4+} $3d_{5/2}$ (u"') and Ce^{4+} $3d_{3/2}$ (v"') peaks appear at binding energy of 917.5 and 897.4 eV, meanwhile Ce^{3+} $3d_{3/2}$ (u°) and Ce^{3+} $3d_{5/2}$ (v°) peaks appear at binding energy of 900.2 and 881.8 eV. This binding energy value is similar to previous studies [23, 26, 44]. The peak intensity ratio of Ce^{3+}/Ce^{4+} was calculated from the ratio of area under peak Ce^{3+} $3d_{5/2}$ (v°) and Ce^{4+} $3d_{5/2}$ (u"'). For BCP/Ce4 and BCP/Ce10 samples, the ratio of Ce^{3+}/Ce^{4+} was counted as 2.49 and 2.15, respectively. This means that BCP/Ce surface can act as a regenerative antioxidant.

3.4 SEM-EDS analysis

Analysis with SEM at a magnification of 50,000 times shows a significant difference in particle morphology for BCP/Ce0 and BCP/Ce4-BCP/Ce12 (Fig. 8). BCP/Ce0 contains plate-like shape particles with a dimension of <100 nm width and about 50–300 nm length. For the BCP/Ce4, spherical particles have a 150–300 nm diameter, but plate-like particles with a size of <100 nm also appear.

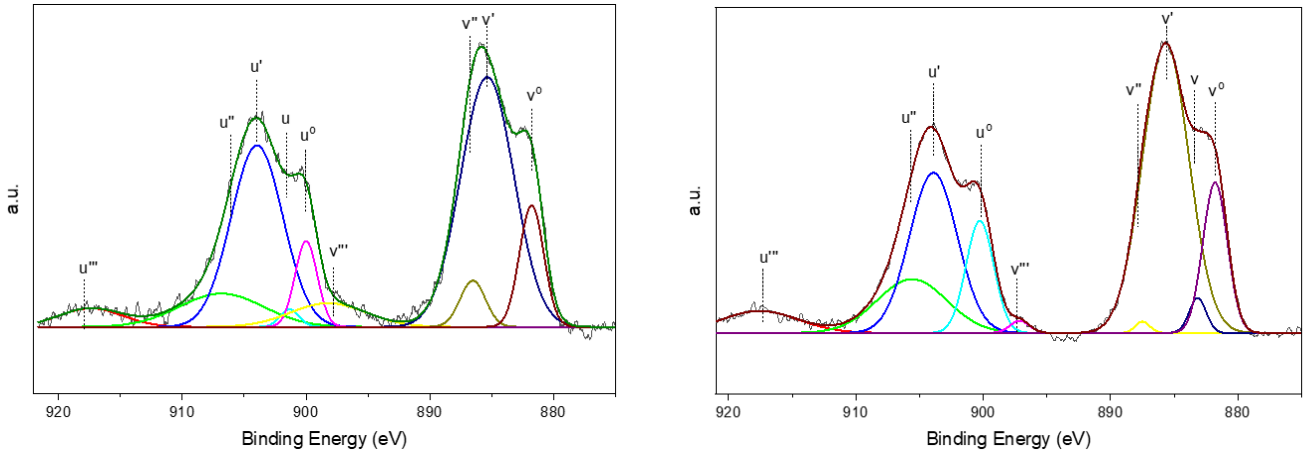

Fig. 7 The fitted curve of Ce *3d* for BCP/Ce4 (a) and BCP/Ce10 (b)

Table 3 The binding energy of Ce *3d* for BCP/Ce4 and BCP/Ce10

Peak	Binding Energy (eV)	
	BCP/Ce4	BCP/Ce10
V	-	883.2
U	901.3	901.7
v''	886.5	887.5
u''	906.8	905.4
v'''	898.2	897.4
u'''	917.4	917.5
v°	881.8	881.8
u°	900.0	900.2
v'	885.4	885.7
u'	904.0	903.9

The number of plate-like particles decreases as the Ce concentration of reactant increases to 8% at the BCP/Ce8. The image of the BCP/Ce10 is dominated by spherical particles with a diameter of <100 nm. Particles with the most uniform shape and size were found in the BCP/Ce12.

The uniform particle formation was driven by the strong interaction of Ca^{2+} ions with cationic N of CTAB molecules. The effective nucleation occurred on the surface of the CTAB micelles. Then the particles grew between the micelles. CTAB has acted as a morphology-directing agent in previous research [32]. SEM image of BCP/Ce4 - BCP/Ce12 showed that Ce's presence in β-TCP structure caused a change in particle shape from plate-like to spherical, with particle size inversely proportional to Ce content. The number of plate-like particles decreases as the Ce concentration increase. Particles of BCP/Ce10 are detected to have the smallest diameter of <100 nm, while the refinement resulted in an average crystallite size of 113.26 nm. The change of the particle shape from plate-like to spherical indicates that Ce^{3+} and Ce^{4+} ions tend to be on the lattice surface [45]. Ce^{3+} ions have a slightly larger diameter (0.107 nm) than Ca^{2+} ions (0.100 nm) [21], so distortion occurs to the particle surface, and the particle size becomes smaller as the Ce content increases.

Analysis of element composition on synthesized BCP/Ce surfaces was conducted with EDS, and the result is presented in Fig. 9. Ca substitution with Ce into the β-TCP structure causes a change in surface element composition. The O concentration tends to increase at BCP/Ce4 and BCP/Ce8 and then falls below the O concentration on β-TCP for BCP/Ce10 and BCP/Ce12. The Ca concentration decreases for BCP/Ce4, BCP/Ce8, and BCP/Ce10 due to Ce's presence. The P concentration relatively does not change for all samples. The Ce concentration in the synthesized BCP/Ce surface increased with the increase in the reactant solution.

The Ca/P and (Ca + Ce)/P ratio of synthesized BCP/Ce can be seen in Table 4. BCP/Ce0 has a Ca/P molar ratio of 1.68, close to the HA molar ratio of 1.67. The presence of Ce reduces the Ca/P ratio, but the (Ca + Ce)/P ratio is still close to the HA molar ratio. This indicates that Ce is mainly found on the surface. Different data were shown by BCP/Ce12 samples where the ratio of Ca/P and ratio (Ca + Ce)/P > of the molar ratio of HA, which indicates that at higher Ce, Ca and Ce are more exposed to the surface.

Element mapping on the surface of the BCP/Ce4 and BCP/Ce10 can be seen in Fig. 10. Consistent with EDS data, on BCP/Ce surface, Ca element (red dots), P element (blue dots), and Ce element (yellow dots) are evenly distributed on the surface. O element (green dots) looks unevenly distributed with the increase of Ce content. Ca Substitution with Ce in the β-TCP structure caused a change in surface element composition. Element mapping indicates that Ce

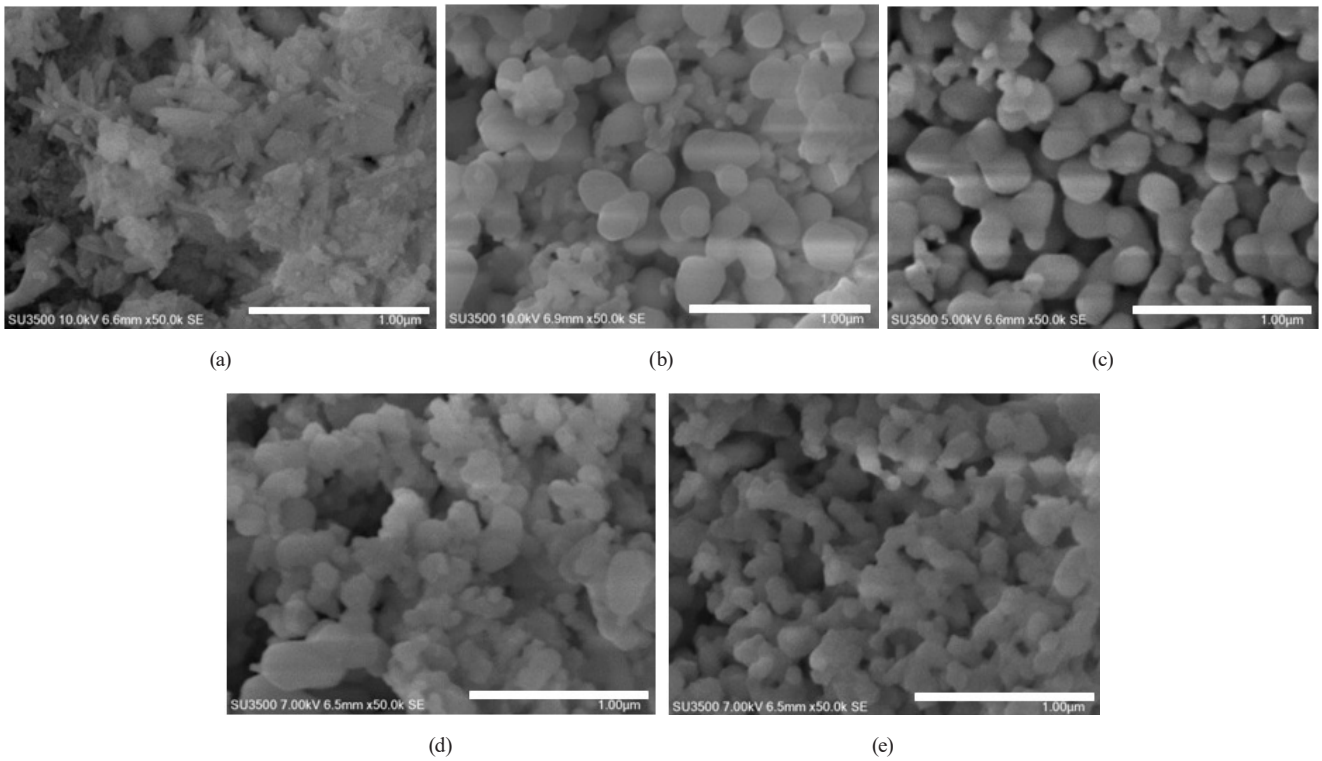

Fig. 8 SEM image of BCP/Ce0 (a), BCP/Ce4 (b), BCP/Ce8 (c), BCP/Ce10 (d), and BCP/Ce12 (e)

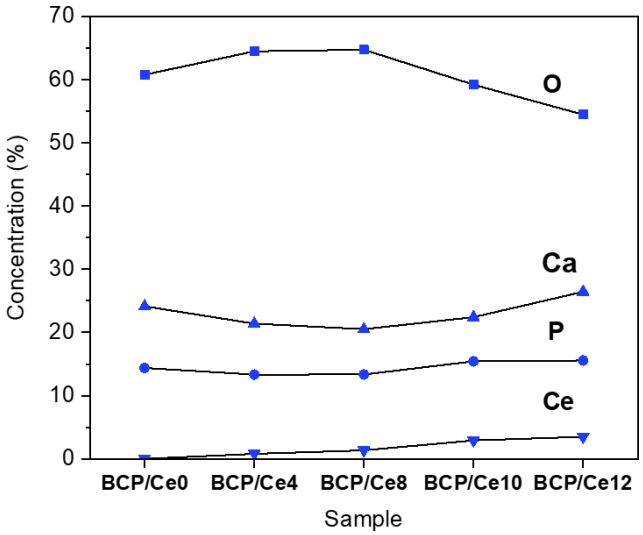

Fig. 9 Element composition on the product surface

Table 4 Ce content, Ca/P ratio, and (Ca + Ce)/P ratio on the sample surface

Sample	[Ce] (%)	Ca/P Ratio	(Ca + Ce)/P Ratio
BCP/Ce0	0.00	1.68	1.68
BCP/Ce4	0.79	1.61	1.66
BCP/Ce8	1.35	1.54	1.64
BCP/Ce10	2.92	1.45	1.64
BCP/Ce12	3.45	1.70	1.92

was distributed evenly on the BCP/Ce surface. The substitution of Ca^{2+} ions with Ce^{3+} and Ce^{4+} ions was compensated with oxygen vacancies. This is confirmed by mapping the oxygen element showing an uneven surface as the Ce concentration increased. The rough surface may act as a catalyst site where the oxidation-reduction reaction occurs [21]. This data indicated that BCP/Ce has an attractive surface reactivity. The Ca^{2+} ions were replaced by Ce^{3+} and Ce^{4+} ions at the lower Ce concentration. In contrast, the excess Ce tends to form $CePO_4$ rather than substitute as much Ca is available at the higher Ce concentration. The EDS data showed that the Ce content on the BCP/Ce10 surface was 2.92%, while the measurement with XPS counted 3.28 ± 0.18%.

3.5 TEM analysis

Further morphology analysis with TEM gave a consistent result with SEM analysis. The SAED pattern indicated that BCP/Ce0 particles have high crystallinity. BCP/Ce4 has a more apparent SAED pattern than BCP/Ce10, or the crystallinity of BCP/Ce4 is greater than BCP/Ce10. The surface distortion changed ions arrangement leading to a decrease in crystallinity, as confirmed by the SAED pattern (Fig. 11). For biomaterial applications, low crystallinity supports biocompatibility due to the increase of bio-resorption property [46]. The spherical shape of BCP/Ce particles is beneficial when used as a powder component of injectable calcium phosphate cement (CPC) [19, 20]. The spherical shape may produce

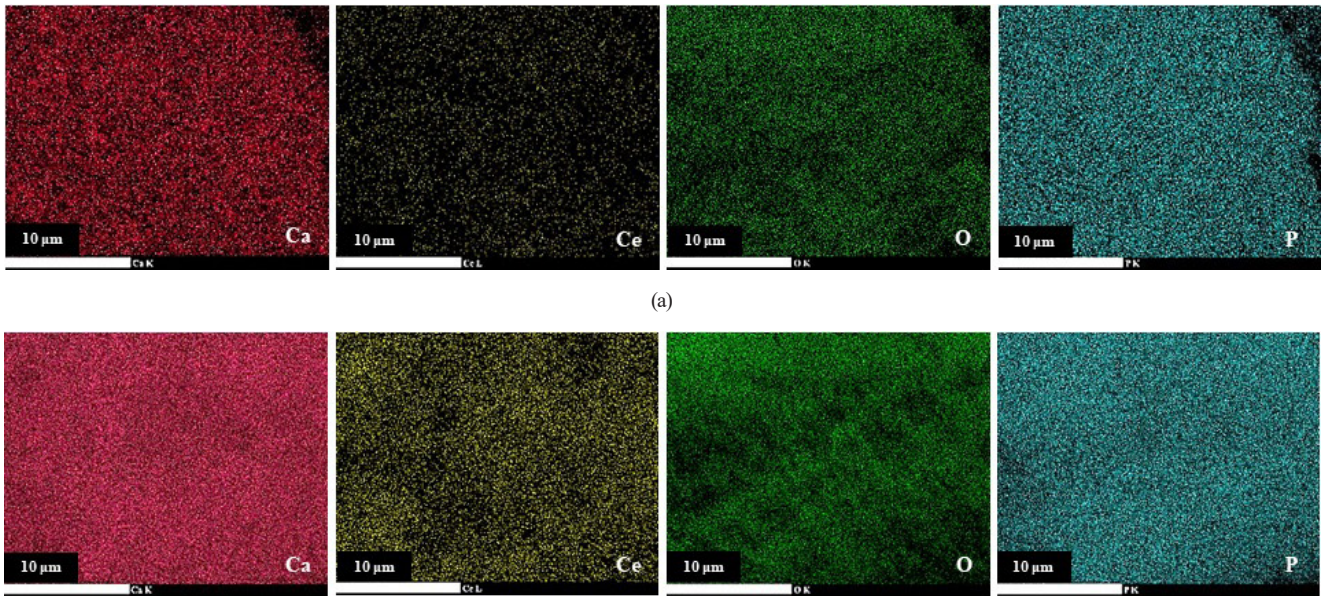

Fig. 10 Element mapping on BCP/Ce4 (a) and BCP/Ce10 (b) surface

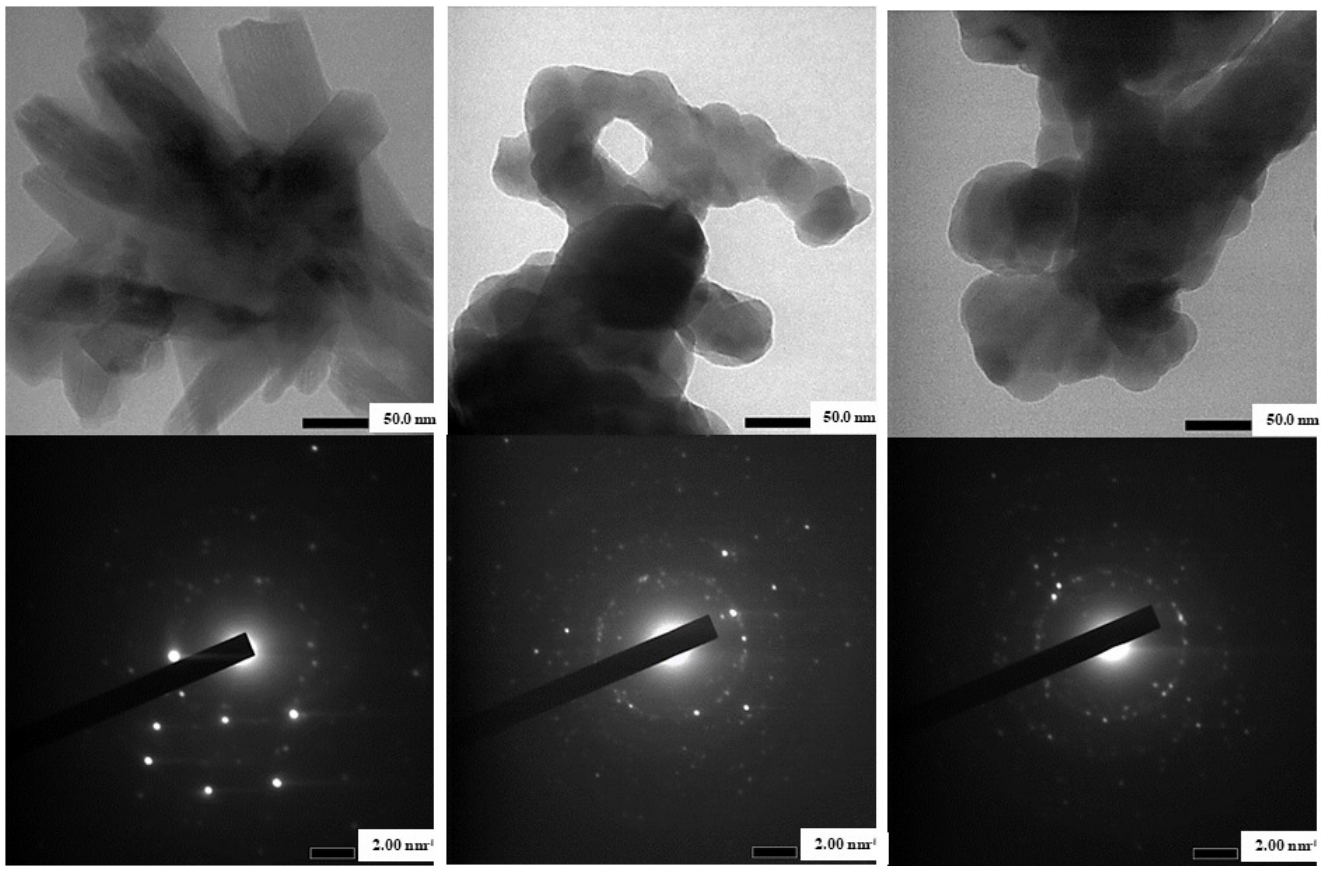

Fig. 11 TEM image and SAED pattern of BCP/Ce0 (a), BCP/Ce4 (b), and BCP/Ce10 (c)

smaller friction between particle-particle and particle-syringe walls so that the viscosity of CPC paste becomes lower. The particle size of BCP/Ce10 may support its biocompatibility because minerals in human bones have dimensions of 40 nm in length, 10 nm in width, and 1–3 nm in thickness [47].

3.6 SF analysis

The photoluminescent test was carried out for BCP/Ce4 and BCP/Ce10 using an emitter at λ = 250 nm. Peaks that are specific to Ce's emission have appeared at λ_{max} of 330–400 nm (near UV region) (Fig. 12 (a)). The emission of light's wavelength depends on the emitter's wavelength [22]. Peak deconvolution can be seen in Fig. 12 (b), (c), in which, for both samples, deconvolution produced four peaks. For the BCP/Ce4, the four peaks appear at λ_{max} at 336.3, 345.5, 366.8, and 388.5 nm. Whereas for the BCP/Ce10, λ_{max} appears at 336.3, 345.8, 368.4, and 397.6 nm. These results are almost the same as the emission phenomena of HA/Ce [25], and Ce substituted calcium pyrophosphate (CPP/Ce) [48].

Emitter light causes electrons Ce^{3+} ions to be excited from 4f orbitals to 5d orbitals. Then unstable condition in 5d orbitals drives the electrons to recombine to initial orbitals by emitting light in the near UV region. The intensity of emission light is not proportional to the Ce content. The BCP/Ce4 exhibits the highest luminescent intensity. This happens since Ce's substituting Ca ions into the β-TCP structure generates oxygen vacancies or crystal defects [22]. As a result, when the electrons are excited to 5d orbitals, some are trapped in oxygen vacancies or crystal defects and do not experience direct recombination to the 4f orbitals. The higher the Ce^{3+} ions concentration, the more oxygen vacancies or crystal defects are available, and the less emission intensity is released. Moreover, the lower the photoluminescence intensity, the more photo excited and electrons can participate in the redox reaction. As reported by Huang et al. [49], a similar phenomenon occurs for HA/Ce samples.

3.7 Zeta potential testing

For the BTCP/Ce0 sample, the Zeta potential value is 0.56 mV, which means that the particles tend to agglomerate in the water. The substitution of Ce causes the average Zeta potential value to change from positive to negative, or the surface is negatively charged, except for the BTCP/Ce0.5 sample (Fig. 13). All BTCP/Ce samples also have low stability in water because the Zeta potential is below 40 mV, which is in the range of 0.71–(−6.14) mV. The negative value of Zeta potential is very supportive if BTCP/Ce is used as a powder component in the production of CPC. Positive charge ions such as Ca^{2+} in body fluids will easily be attached to the CPC surface. The attachment of Ca^{2+} ions will be followed by PO_4^{3-} ions so that the resorptive-formative process can be done and new bone tissue

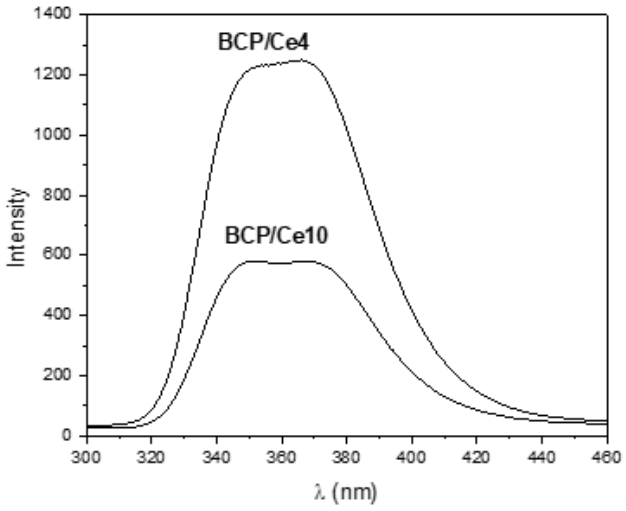

(a)

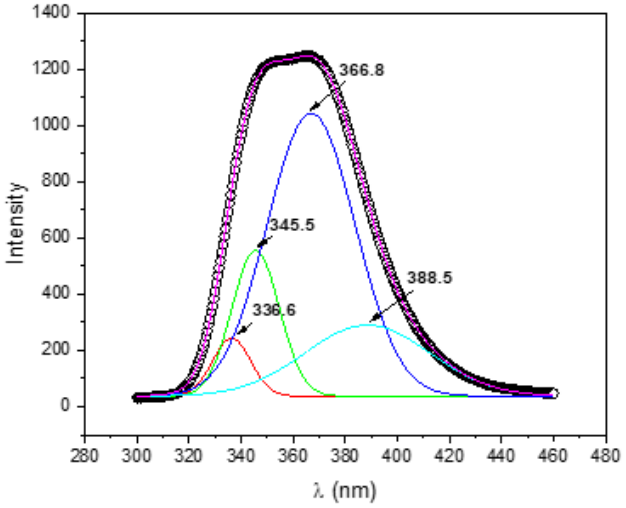

(b)

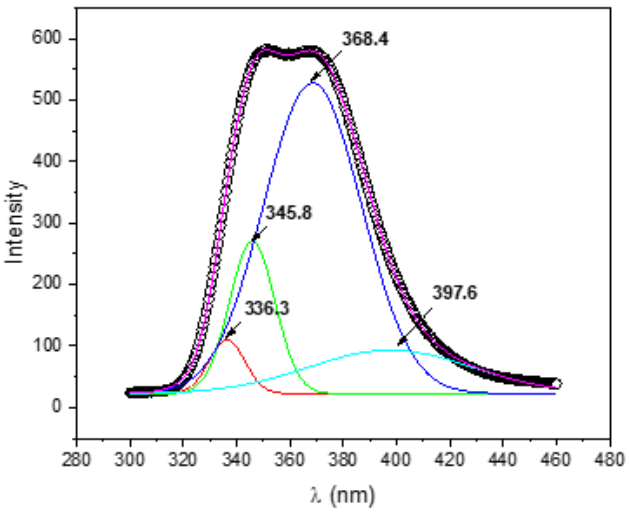

(c)

Fig. 12 Photoluminescent spectra of BCP/Ce4 and BCP/Ce10 (a), deconvolution peaks of BCP/Ce4 (b) and BCP/Ce10 (c)

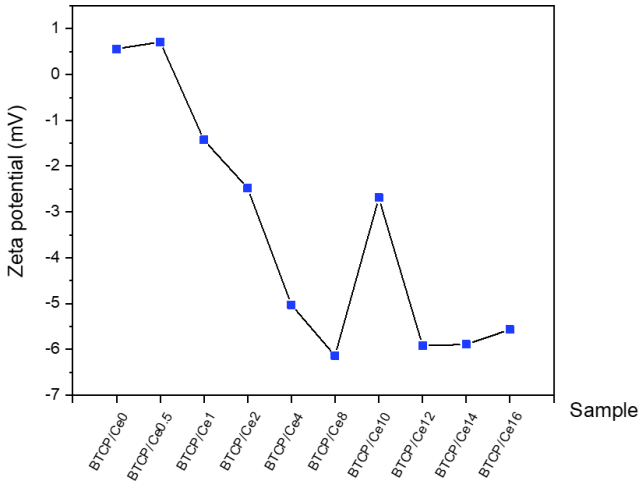

Fig. 13 Zeta potential of BCP/Ce

can be formed. A negative Zeta potential value is also required for bone cell adhesion [50]. Thus, using BTCP/Ce as a powder component of CPC can promote osteointegration, apatite nucleation, and bone regeneration [51].

4 Conclusion

The BCP substituted Ce (BCP/Ce) by a sol-gel method as a potential osteoporotic bone filler had been successfully synthesized and characterized. The influence of Ce as a precursor was also investigated. The presence of Ce in the synthesis of BCP increased the ratio of β-TCP over HA. HA can sustain its structure, while Ce isomorphically substitutes β-TCP structure at the Wyckoff site of 6a (0,0,-0.085) or the Ca (4) position. Ce also affects the particle's shape and size as well as the surface charge and luminescent property of BCP that support the ability of the BCP/Ce to be used as a powder component of calcium phosphate cement.

Acknowledgments

The authors gratefully acknowledge The Ministry of Research, Technology, and Higher Education and The Ministry of the Finance Republic of Indonesia for the financial research support through BUDI-DN LPDP Project.

References

[1] Kaur, G. "Clinical applications of biomaterials: State-of-the-art progress, trends, and novel approaches", Springer International Publishing, 2017. ISBN 978-3-319-56058-8 https://doi.org/10.1007/978-3-319-56059-5

[2] Kunert-Keil, C., Scholz, F., Gedrange, T., Gredes, T. "Comparative study of biphasic calcium phosphate with beta-tricalcium phosphate in rat cranial defects—A molecular-biological and histological study", Annals of Anatomy - Anatomischer Anzeiger, 199, pp. 79–84, 2015. https://doi.org/10.1016/j.aanat.2013.12.001

[3] Ebrahimi, M., Botelho, M. "Biphasic calcium phosphates (BCP) of hydroxyapatite (HA) and tricalcium phosphate (TCP) as bone substitutes: Importance of physicochemical characterizations in biomaterials studies", Data in Brief, 10, pp. 93–97, 2017. https://doi.org/10.1016/j.dib.2016.11.080

[4] Bauer, L., Antunović, M., Rogina, A., Ivanković, M., Ivanković, H. "Bone-mimetic porous hydroxyapatite/whitlockite scaffolds: preparation, characterization and interactions with human mesenchymal stem cells", Journal of Materials Science, 56(5), pp. 3947–3969, 2021. https://doi.org/10.1007/s10853-020-05489-3

[5] Bohner, M., Lemaitre, J. "Can bioactivity be tested in vitro with SBF solution?", Biomaterials, 30(12), pp. 2175–2179, 2009. https://doi.org/10.1016/j.biomaterials.2009.01.008

[6] Zerbo, I. R., Bronckers, A. L. J. J., de Lange, G., Burger, E. H. "Localisation of osteogenic and osteoclastic cells in porous β-tricalcium phosphate particles used for human maxillary sinus floor elevation", Biomaterials, 26(12), pp. 1445–1451, 2005. https://doi.org/10.1016/j.biomaterials.2004.05.003

[7] Kondo, N., Ogose, A., Tokunaga, K., Ito, T., Arai, K., Kudo, N., Inoue, H., Irie, H., Endo, N. "Bone formation and resorption of highly purified β-tricalcium phosphate in the rat femoral condyle", Biomaterials, 26(28), pp. 5600–5608, 2005. https://doi.org/10.1016/j.biomaterials.2005.02.026

[8] Okuda, T., Ioku, K., Yonezawa, I., Minagi, H., Kawachi, G., Gonda, Y., Murayama, H., Shibata, Y., Minami, S., Kamihira, S., Kurosawa, H., Ikeda, T. "The effect of the microstructure of β-tricalcium phosphate on the metabolism of subsequently formed bone tissue", Biomaterials, 28(16), pp. 2612–2621, 2007. https://doi.org/10.1016/j.biomaterials.2007.01.040

[9] Yamada, S., Heymann, D., Bouler, J.-M., Daculsi, G. "Osteoclastic resorption of calcium phosphate ceramics with different hydroxyapatite/β-tricalcium phosphate ratios", Biomaterials, 18(15), pp. 1037–1041, 1997. https://doi.org/10.1016/S0142-9612(97)00036-7

[10] Kim, D.-H., Kim, K.-L., Chun, H.-H., Kim, T.-W., Park, H.-C., Yoon, S.-Y. "In vitro biodegradable and mechanical performance of biphasic calcium phosphate porous scaffolds with unidirectional macro-pore structure", Ceramics International, 40(6), pp. 8293–8300, 2014. https://doi.org/10.1016/j.ceramint.2014.01.031

[11] Schumacher, M., Deisinger, U., Detsch, R., Ziegler, G. "Indirect rapid prototyping of biphasic calcium phosphate scaffolds as bone substitutes: influence of phase composition, macroporosity and pore geometry on mechanical properties", Journal of Materials Science: Materials in Medicine, 21(12), pp. 3119–3127, 2010. https://doi.org/10.1007/s10856-010-4166-6

[12] Marques, C. F., Perera, F. H., Marote, A., Ferreira, S., Vieira, S. I., Olhero, S., Miranda, P., Ferreira, J. M. F. "Biphasic calcium phosphate scaffolds fabricated by direct write assembly: Mechanical, anti-microbial and osteoblastic properties", Journal of the European Ceramic Society, 37(1), pp. 359–368, 2017. https://doi.org/10.1016/j.jeurceramsoc.2016.08.018

[13] Garai, S., Sinha, A. "Three dimensional biphasic calcium phosphate nanocomposites for load bearing bioactive bone grafts", Materials Science and Engineering: C, 59, pp. 375–383, 2016. https://doi.org/10.1016/j.msec.2015.10.027

[14] Silva, F. R. O., Lima, N. B., Guilhen, S. N., Courrol, L. C., Bressiani, A. H. A. "Evaluation of europium-doped HA/β-TCP ratio fluorescence in biphasic calcium phosphate nanocomposites controlled by the pH value during the synthesis", Journal of Luminescence, 180, pp. 177–182, 2016. https://doi.org/10.1016/j.jlumin.2016.08.030

[15] Kim, T.-W., Lee, H.-S., Kim, D.-H., Jin, H.-H., Hwang, K.-H., Lee, J. K., Park, H.-C., Yoon, S.-Y. "In situ synthesis of magnesium-substituted biphasic calcium phosphate and in vitro biodegradation", Materials Research Bulletin, 47(9), pp. 2506–2512, 2012. https://doi.org/10.1016/j.materresbull.2012.05.011

[16] Sopyan, I., Ramesh, S., Nawawi, N. A., Tampieri, A., Sprio, S. "Effects of manganese doping on properties of sol-gel derived biphasic calcium phosphate ceramics", Ceramics International, 37(8), pp. 3703–3715, 2011. https://doi.org/10.1016/j.ceramint.2011.06.033

[17] Gomes, S., Kaur, A., Grenèche, J.-M., Nedelec, J.-M., Renaudin, G. "Atomic scale modeling of iron-doped biphasic calcium phosphate bioceramics", Acta Biomaterialia, 50, pp. 78–88, 2017. https://doi.org/10.1016/j.actbio.2016.12.011

[18] Zhou, G., Li, Y., Zheng, B., Wang, W., Gao, J., Wei, H., Li, S., Wang, S., Zhang, J. "Cerium oxide nanoparticles protect primary osteoblasts against hydrogen peroxide induced oxidative damage", Micro & Nano Letters, 9(2), pp. 91–96, 2014. https://doi.org/10.1049/mnl.2013.0586

[19] Torres, P. M. C., Gouveia, S., Olhero, S., Kaushal, A., Ferreira, J. M. F. "Injectability of calcium phosphate pastes: Effects of particle size and state of aggregation of β-tricalcium phosphate powders", Acta Biomaterialia, 21, pp. 204–216, 2015. https://doi.org/10.1016/j.actbio.2015.04.006

[20] Bae, J., Ida, Y., Sekine, K., Kawano, F., Hamada, K. "Effects of high-energy ball-milling on injectability and strength of β-tricalcium-phosphate cement", Journal of the Mechanical Behavior of Biomedical Materials, 47, pp. 77–86, 2015. https://doi.org/10.1016/j.jmbbm.2015.03.005

[21] Hirst, S. M., Karakoti, A. S., Tyler, R. D., Sriranganathan, N., Seal, S., Reilly, C. M. "Anti-inflammatory properties of cerium oxide nanoparticles", Small, 5(24), pp. 2848–2856, 2009. https://doi.org/10.1002/smll.200901048

[22] Khan, M. E., Khan, M. M., Cho, M. H. "Ce^{3+}-ion, surface oxygen vacancy, and visible light-induced photocatalytic dye degradation and photocapacitive performance of CeO_2-graphene nanostructures", Scientific Reports, 7, 5928, 2017. https://doi.org/10.1038/s41598-017-06139-6

[23] Pandey, A., Midha, S., Kumar, R. K., Maurya, R., Kumar, V. K., Ghosh, S., Balani, K. "Antioxidant and antibacterial hydroxyapatite-based biocomposite for orthopedic applications", Materials Science and Engineering: C, 88, pp. 13–24, 2018. https://doi.org/10.1016/j.msec.2018.02.014

[24] Feng, Z., Liao, Y., Ye, M. "Synthesis and structure of cerium-substituted hydroxyapatite", Journal of Materials Science: Materials in Medicine, 16(5), pp. 417–421, 2005. https://doi.org/10.1007/s10856-005-6981-8

[25] Ciobanu, C. S., Popa, C. L., Predoi, D. "Cerium doped hydroxyapatite nanoparticles synthesized by co-precipitation method", Journal of the Serbian Chemical Society, 81(4), pp. 433–446, 2016. https://doi.org/10.2298/JSC150824007C

[26] Nandha Kumar, P., Mishra, S. K., Kannan, S. "Structural perceptions and mechanical evaluation of β-$Ca_3(PO_4)_2$/c-CeO_2 composites with preferential occupancy of Ce^{3+} and Ce^{4+}", Inorganic Chemistry, 56(6), pp. 3600–3611, 2017. https://doi.org/10.1021/acs.inorgchem.7b00045

[27] Phatai, P., Futalan, C. M., Utara, S., Khemthong, P., Kamonwannasit, S. "Structural characterization of cerium-doped hydroxyapatite nanoparticles synthesized by an ultrasonic-assisted sol-gel technique", Results in Physics, 10, pp. 956–963, 2018. https://doi.org/10.1016/j.rinp.2018.08.012

[28] Gražulis, S., Chateigner, D., Downs, R. T., Yokochi, A. F. T., Quirós, M., Lutterotti, L., Manakova, E., Butkus, J., Moeck, P., Le Bail, A. "Crystallography open database - An open-access collection of crystal structures", Journal of Applied Crystallography, 42(4), pp. 726–729, 2009. https://doi.org/10.1107/S0021889809016690

[29] Gražulis, S., Daškevič, A., Merkys, A., Chateigner, D., Lutterotti, L., Quirós, M., Serebryanaya, N. R., Moeck, P., Downs, R. T., Le Bail, A. "Crystallography open database (COD): an open-access collection of crystal structures and platform for world-wide collaboration", Nucleic Acids Research, 40(D1), pp. D420–D427, 2012. https://doi.org/10.1093/nar/gkr900

[30] Bohner, M., Santoni, B. L. G., Döbelin, N. "β-tricalcium phosphate for bone substitution: Synthesis and properties", Acta Biomaterialia, 113, pp. 23–41, 2020. https://doi.org/10.1016/j.actbio.2020.06.022

[31] Windarti, T., Darmawan, A., Marliana, A. "Synthesis of β-TCP by sol-gel method: Variation of Ca/P molar ratio", IOP Conference Series: Materials Science and Engineering, 509, 012147, 2019. https://doi.org/10.1088/1757-899X/509/1/012147

[32] Shiba, K., Motozuka, S., Yamaguchi, T., Ogawa, N., Otsuka, Y., Ohnuma, K., Kataoka, T., Tagaya, M. "Effect of cationic surfactant micelles on hydroxyapatite nanocrystal formation: An investigation into the inorganic−organic interfacial interactions", Crystal Growth & Design, 16(3), pp. 1463–1471, 2016. https://doi.org/10.1021/acs.cgd.5b01599

[33] Lutterotti, L., Matthies, S., Wenk, H. R. "MAUD: A friendly java program for material analysis using diffraction", Commision on Powder Diffraction Newsletter, 21, pp. 14–15, 1999.

[34] Merkys, A., Vaitkus, A., Butkus, J., Okulič-Kazarinas, M., Kairys, V., Gražulis, S. "*COD::CIF::Parser*: An error-correcting CIF parser for the Perl language", Journal of Applied Crystallography, 49(1), pp. 292–301, 2016. https://doi.org/10.1107/S1600576715022396

[35] Quirós, M., Gražulis, S., Girdzijauskaitė, S., Merkys, A., Vaitkus, A. "Using SMILES strings for the description of chemical connectivity in the Crystallography Open Database", Journal of Cheminformatics, 10(1), 23, 2018. https://doi.org/10.1186/s13321-018-0279-6

[36] Gražulis, S., Merkys, A., Vaitkus, A., Okulič-Kazarinas, M. "Computing stoichiometric molecular composition from crystal structures", Journal of Applied Crystallography, 48(1), pp. 85–91, 2015. https://doi.org/10.1107/S1600576714025904

[37] Berzina-Cimdina, L., Borodajenko, N. "Research of calcium phosphates using fourier transform infrared spectroscopy", In: Theophanides, T. (ed.) Infrared Spectroscopy - Materials Science, Engineering and Technology, IntechOpen, 2012, pp. 123–148. ISBN 978-953-51-0537-4

[38] Zhu, G., Zhao, R., Li, Y., Tang, R. "Multifunctional Gd, Ce, Tb co-doped β-tricalcium phosphate porous nanospheres for sustained drug release and bioimaging", Journal of Materials Chemistry B, 4(22), pp. 3903–3910, 2016. https://doi.org/10.1039/C5TB02767E

[39] Choudhury, B., Chetri, P., Choudhury, A. "Annealing temperature and oxygen-vacancy-dependent variation of lattice strain, band gap and luminescence properties of CeO_2 nanoparticles", Journal of Experimental Nanoscience, 10(2), pp. 103–114, 2015. https://doi.org/10.1080/17458080.2013.801566

[40] Dorozhkin, S. V. "Calcium orthophosphate bioceramics", Ceramics International, 41(10), pp. 13913–13966, 2015. https://doi.org/10.1016/j.ceramint.2015.08.004

[41] Yashima, M., Sakai, A., Kamiyama, T., Hoshikawa, A. "Crystal structure analysis of β-tricalcium phosphate $Ca_3(PO_4)_2$ by neutron powder diffraction", Journal of Solid State Chemistry, 175(2), pp. 272–277, 2003. https://doi.org/10.1016/S0022-4596(03)00279-2

[42] Shannon, R. D., Prewitt, C. T. "Effective ionic radii in oxides and fluorides", Acta Crystallographica Section B: Structural Science, Crystal Engineering and Materials, B25(5), pp. 925–946, 1969. https://doi.org/10.1107/s0567740869003220

[43] Janoš, P., Hladík, T., Kormunda, M., Ederer, J., Šťastný, M. "Thermal treatment of cerium oxide and its properties: Adsorption ability versus degradation efficiency", Advances in Materials Science and Engineering, 2014, 706041, 2014. https://doi.org/10.1155/2014/706041

[44] Li, K., Shen, Q., Xie, Y., You, M., Huang, L., Zheng, X. "Incorporation of cerium oxide into hydroxyapatite coating protects bone marrow stromal cells against H_2O_2-induced inhibition of osteogenic differentiation", Biological Trace Element Research, 182(1), pp. 91–104, 2018. https://doi.org/10.1007/s12011-017-1066-3

[45] Priyadarshini, B., Anjaneyulu, U., Vijayalakshmi, V. "Preparation and characterization of sol-gel derived Ce^{4+} doped hydroxyapatite and its in vitro biological evaluations for orthopedic applications", Materials and Design, 119, pp. 446–455, 2017. https://doi.org/10.1016/j.matdes.2017.01.095

[46] Denry, I., Kuhn, L.T. "Design and characterization of calcium phosphate ceramic scaffolds for bone tissue engineering", Dental Materials, 32(1), pp. 43–53, 2016. https://doi.org/10.1016/j.dental.2015.09.008

[47] Florencio-Silva, R., Sasso, G. R. S., Sasso-Cerri, E., Simões, M. J., Cerri, P. S. "Biology of bone tissue: Structure, function, and factors that influence bone cells", BioMed Research International, 2015, 421746, 2015. https://doi.org/10.1155/2015/421746

[48] Lozano, I. B., Roman-Lopez, J., Sosa, R., Díaz-Góngora, J. A. I., Azorín, J. "Preparation of cerium doped calcium pyrophosphate: Study of luminescent behavior", Journal of Luminescence, 173, pp. 5–10, 2016. https://doi.org/10.1016/j.jlumin.2015.12.032

[49] Huang, W., Mao, Z., Chen, L., Chi, Y., Jiang, H., Zimba, B. L., Xiong, G., Wu, Q. "Synthesis and characterisation of fluorescent and biocompatible hydroxyapatite nanoparticles with cerium doping", Micro & Nano Letters, 13(5), pp. 699–703, 2018. https://doi.org/10.1049/mnl.2017.0729

[50] Fahami, A., Beall, G. W., Betancourt, T. "Synthesis, bioactivity and zeta potential investigations of chlorine and fluorine substituted hydroxyapatite", Materials Science and Engineering: C, 59, pp. 78–85, 2016. https://doi.org/10.1016/j.msec.2015.10.002

[51] Latifi, S. M., Fathi, M., Sharifnabi, A., Varshosaz, J. "*In vitro* characterisation of a sol–gel derived *in situ* silica-coated silicate and carbonate co-doped hydroxyapatite nanopowder for bone grafting", Materials Science and Engineering: C, 75, pp. 272–278, 2017. https://doi.org/10.1016/j.msec.2017.02.078